

The Dust Extinction Curve: Beyond $R(V)$

GREGORY M. GREEN ¹, XIANGYU ZHANG (张翔宇) ¹ AND RUOYI ZHANG (张若羿) ^{2,1}

¹*Max-Planck-Institut für Astronomie*

Königstuhl 17, D-69117 Heidelberg, Germany

²*School of Physics and Astronomy, Beijing Normal University,*

No.19, Xijiekouwai St, Haidian District, Beijing 100875, People's Republic of China

ABSTRACT

The dust extinction curve is typically parameterized by a single variable, $R(V)$, in optical and near-infrared wavelengths. $R(V)$ controls the slope of the extinction-vs.-wavelength curve, and is thought to reflect the grain-size distribution and composition of dust. Low-resolution, flux-calibrated BP/RP spectra from Gaia have allowed the determination of the extinction curve along sightlines to 130 million stars in the Milky Way and Magellanic Clouds. We show that these extinction curves contain more than a single degree of freedom – that is, that they are not simply described by $R(V)$. We identify a number of components that are orthogonal to $R(V)$ variation, and show that these components vary across the sky in coherent patterns that resemble interstellar medium structure. These components encode variation in the 770 nm extinction feature, intermediate-scale and very broad structure, and a newly identified feature at 850 nm, and likely trace both dust composition and local conditions in the interstellar medium. Correlations of the 770 nm and 850 nm features with $R(V)$ suggest that their carriers become more abundant as the carrier of the 2175 Å feature is destroyed. Our 24 million extinction-curve decompositions and feature equivalent-width measurements are publicly available at DOI:10.5281/zenodo.14005028.

Keywords: Interstellar dust (836) — Interstellar dust extinction (837) — Interstellar medium (847) — Polycyclic aromatic hydrocarbons (1280) — Principal component analysis (1944)

1. INTRODUCTION

Dust extinction as a function of wavelength (the extinction curve) is diagnostic of the chemical composition and size distribution of dust grains. Historically, the shape of the extinction curve in the Milky Way has been described by a single parameter, $R(V) \equiv A(V)/E(B-V)$, which is the ratio of extinction in the V band to reddening in $B-V$ bands (*e.g.*, Cardelli et al. 1989; Fitzpatrick 1999; Gordon et al. 2023). If this single parameter is sufficient to describe all extinction curves throughout the Galaxy, then that suggests that the composition of the dust anywhere in the Galaxy can likewise be described by a single parameter. In this picture, all dust populations would exist somewhere along a one-dimensional continuum, with one extreme being a bottom-heavy (a higher proportion of small dust grains), low- $R(V)$ population, and the other extreme being a top-heavy, high- $R(V)$ population. There is already evidence against this simplistic paradigm from the ultraviolet (UV), where $R(V)$ has

been found to be insufficient to capture all Milky Way extinction-curve variation (Peek & Schiminovich 2013). Additional evidence against this paradigm comes from Zhang & Green (2024), which found that high $R(V)$ tends to occur in two very different physical regimes, the diffuse interstellar medium (ISM) and dense molecular clouds, with low $R(V)$ occurring at intermediate densities. The differing conditions in these two high- $R(V)$ regimes could leave some imprint on the extinction curve – that is, variations that cannot be captured by $R(V)$ alone. In this paper, we use 24 million well measured optical extinction curves from Zhang & Green (2024), covering the entire low-Galactic-latitude sky, to test whether one parameter, $R(V)$, really is sufficient to describe all optical extinction curves.

Our approach is to decompose our extinction curves into a small number of components, ordered in some way by statistical significance. We expect the most significant component to represent $R(V)$ variation. Additional components may represent physical changes in

dust composition, systematic errors in the data, or a combination of both.

The idea of decomposing extinction curves into separate components has been applied several times before. [Massa \(1980\)](#) decomposed the UV extinction curve into two components. [Schlafly et al. \(2016\)](#) measured optical-NIR reddening curves (*i.e.*, differences in extinction between different wavelengths) of 37,000 stars using a combination of APOGEE spectroscopy and broadband photometry from Pan-STARRS 1, 2MASS and WISE. [Schlafly et al. \(2017\)](#) used the second principal component from this analysis to map $R(V)$ across the APOGEE footprint. [Massa et al. \(2020, “MFG20”\)](#) identified three statistically significant principal components in optical-UV extinction curves measured by the International Ultraviolet Explorer and Hubble/STIS. MFG20 analyzed the behavior of both the “very broad structure” (VBS), a depression in extinction from roughly 500–670 nm, and “intermediate-scale structure” (ISS), which refers to features in the extinction curve that are wider than diffuse interstellar bands (DIBs) but narrower than the VBS. MFG20 found the strengths of the ISS features at 430, 487 and 630 nm to be uncorrelated with $R(V)$, but found the features at 430 and 487 nm to be correlated with the strength of the 2175 Å extinction bump. Of these ISS features, only the 630 nm feature, which has a FWHM of ~ 11 nm is close to being resolvable in Gaia XP spectra, which have an effective wavelength resolution of ~ 10 nm. More recently, [Maíz Apellániz et al. \(2021\)](#) identified a feature centered on 770 nm, with a FWHM of ~ 17.7 nm. Given the width of this feature, it is a much more promising target for analysis in low-resolution Gaia XP spectra than other, narrower ISS features.

Now, thanks to Gaia XP spectra ([Gaia Collaboration et al. 2016, 2023; De Angeli et al. 2023; Montegriffo et al. 2023](#)) we have enough measured extinction curves – measured densely across the sky – to not only look for statistically significant components of the extinction curve, but to also map their strengths across the sky. This allows correlation between extinction-curve variations and other physical conditions in the interstellar medium (ISM). Sky maps of extinction-curve variation also allow the separation of real, physical variations in the extinction curve from observational artifacts, based on the typical imprints (e.g., dust-like filamentary structure vs. Gaia scanning patterns) on the sky. We believe this combination of spectral and spatial information can be a powerful tool for identifying and determining the physical origin of extinction-curve variations.

2. EMPIRICAL EXTINCTION CURVES

[Zhang & Green \(2024, hereafter “ZG24”\)](#) inferred distances and intrinsic stellar and dust parameters from Gaia XP spectra, based on a data-driven forward model. This resulted in reliable measurements of dust extinction and $R(V)$ along sightlines towards 130 million stars. The ZG24 model treats the dust extinction curve as a single-parameter family of curves, which is determined directly from the data (with weak priors on the continuity of the curves in wavelength space).

However, in this paper, we intend to go beyond the assumption that the shape of the extinction curve is determined by a single parameter. We determine an “empirical” extinction curve for each star by comparing the ZG24 prediction of each star’s intrinsic, zero-extinction spectrum to the observed, extinguished spectrum. To do this, we input the ZG24 estimates of the stellar distance and atmospheric parameters (T_{eff} , $[\text{Fe}/\text{H}]$, $\log g$) into the ZG24 model, assuming zero extinction, obtaining a predicted intrinsic Gaia XP spectrum, \vec{f}_{int} (with each component representing a different wavelength), for each star. In this work, we use only the Gaia XP spectral range of the ZG24 model, which spans 392–992 nm, sampled every 10 nm, for a total of 61 wavelength samples.

Next, we compare these intrinsic spectra to the observed Gaia XP spectra to obtain extinction as a function of wavelength. The observed spectral fluxes contain uncertainties, which the Gaia catalog assumes to be normally distributed. We calculate the covariance matrix of the flux uncertainties for each spectrum identically to ZG24. Including the lowest-order correction for observational uncertainty, the expectation value of extinction at a single wavelength is given by

$$\langle A \rangle \simeq -\frac{2.5}{\ln 10} \left[\ln \left(\frac{\mu_f}{f_{\text{int}}} \right) - \frac{1}{2} \left(\frac{\sigma_f}{\mu_f} \right)^2 \right], \quad (1)$$

where μ_f and σ_f are the mean and standard deviation of observed flux, respectively, at the given wavelength (see Appendix A for a derivation). The covariance matrix of extinction at two wavelengths, λ_i and λ_j , is approximately given by

$$\text{cov}(A_i, A_j) \simeq \left(\frac{2.5}{\ln 10} \right)^2 \left(\frac{\sigma_{f,ij}^2}{\mu_{f,i}\mu_{f,j}} - \frac{1}{4} \frac{\sigma_{f,i}^2 \sigma_{f,j}^2}{\mu_{f,i}^2 \mu_{f,j}^2} \right), \quad (2)$$

where $\sigma_{f,ij}^2$ is the covariance between the observed fluxes at λ_i and λ_j , and $\mu_{f,i}$ and $\sigma_{f,i}$ are the mean and standard deviation, respectively, of the observed flux at wavelength i . We thus obtain an estimate of the extinction of each star and its covariant uncertainties, which we treat as Gaussian.

As we are interested in the *shape* of the extinction curve, independent of the overall amount of extinction,

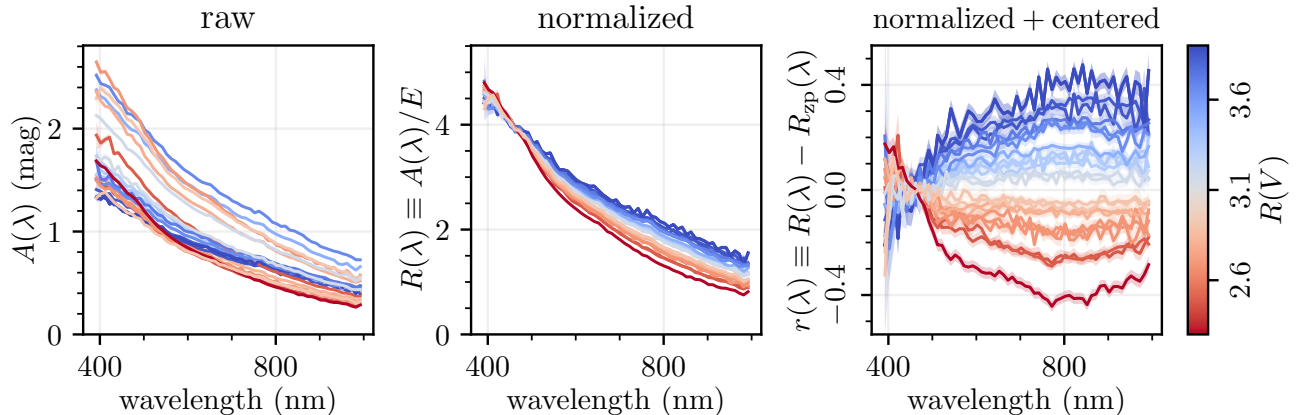


Figure 1. Normalization and centering of our empirical extinction curves. The left panel shows a small subset of our raw, empirical extinction curves, $A(\lambda)$. The middle panel shows the same extinction curves, normalized by the ZG24 estimate of scalar extinction, E , which is similar to $E(B-V)$. The right panel shows the normalized extinction curves, with a reference curve subtracted out. Each extinction curve is colored by its $R(V)$ estimate in ZG24, and shaded envelopes show the $\pm 1\sigma$ uncertainties on each curve. We extract the most significant components of the right extinction curves using our CovPCA algorithm.

we normalize each extinction curve by the ZG24 estimate of the scalar amount of extinction, E : $R(\lambda) \equiv A(\lambda)/E$. We additionally subtract off the mean shape of the curve (averaged over the extinction curves), which we call $R_{zp}(\lambda)$. We will thus look for variation in the normalized and “centered” extinction curves, which we denote by $r(\lambda)$:

$$r(\lambda) \equiv \frac{A(\lambda)}{E} - R_{zp}(\lambda). \quad (3)$$

As we work with Gaia XP spectra sampled at discrete wavelengths, we work with the vector \vec{r} . The covariance matrix of \vec{r} is simply the covariance matrix of \vec{A} , scaled by $1/E^2$.

Fig. 1 illustrates how we transform our raw extinction curves, $A(\lambda)$, into our normalized and centered extinction curves, $r(\lambda)$.

3. DECOMPOSITION OF EXTINCTION CURVES

Our empirical extinction curves are not guaranteed to belong to a single-parameter family, and indeed, our intent is to search for additional variation beyond $R(V)$. We search for a small number of components that, when combined linearly, can match most of our high-quality empirical extinction curves well.

We define “high-quality” (HQ) extinction curves based on the signal-to-noise ratio of the underlying Gaia XP spectra (`phot_X_mean_flux/phot_X_mean_flux_error` > 2500 for $X = \text{bp}$ and rp), the quality of the ZG24 stellar parameter estimates (`quality_flags` < 8 and `teff_confidence` > 0.5), and the ZG24 estimate of scalar extinction ($E > 1$). These cuts select stars for

which the observed and intrinsic spectra are well determined, and for which there is enough extinction to determine the *shape* of the extinction curve. In all, we obtain 29,968 HQ sources.

Our extinction curves reside in a 61-dimensional vector space (with each dimension representing extinction at a different wavelength). We look for a low-dimensional subspace that can explain most of the variation in the extinction curves. In technical terms, we search for a small ($\ll 61$) set of universal basis vectors, as well as coefficients for each extinction curve, which minimize the average χ^2 difference between the extinction curves and their representation in the subspace. This is similar in spirit to Principal Component Analysis (PCA), but with the critical difference that we would like to take into account the covariant uncertainties on each observation.

We represent the basis vectors, which define the subspace, using the matrix \mathbf{G} , which has shape $n_\lambda \times n_b$, where $n_\lambda = 61$ is the number of wavelengths in each extinction curve, and n_b is the dimensionality of our subspace (which we will set to 16 in this work). Each column of \mathbf{G} is thus a basis vector. We represent the coefficients of extinction curve i in this subspace by the vector \vec{b}_i , which is of n_b dimensions. Extinction curve i is thus to be approximated by $\vec{r}_i \simeq \mathbf{G} \vec{b}_i$. We seek to minimize the total χ^2 distance between all the observed extinction curves and their representations in the subspace:

$$\chi^2 = \sum_{\text{star } i} \left(\mathbf{G} \vec{b}_i - \vec{r}_i \right)^T \mathbf{C}_i^{-1} \left(\mathbf{G} \vec{b}_i - \vec{r}_i \right), \quad (4)$$

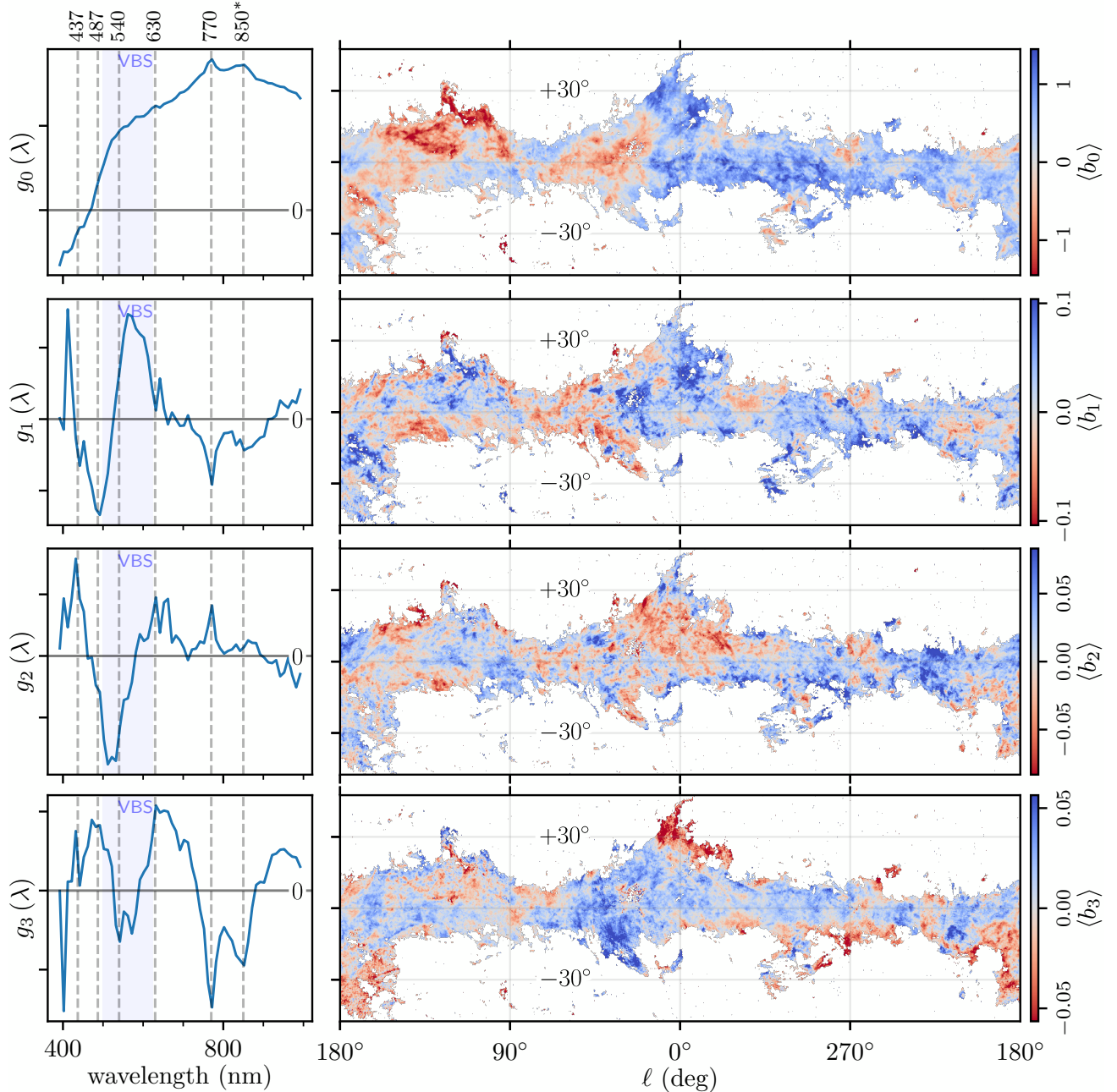


Figure 2. The first four components of the extinction curve (left panels), and corresponding sky maps of their inverse-variance-weighted mean strengths (right panels). We only show regions of the sky for which the inverse-variance-weighted mean extinction, E , is greater than 0.15. The sky maps of these components are relatively free of Gaia scanning-pattern artifacts, and reveal patterns that visually resemble ISM structures. Component 0 is nearly perfectly correlated with $R(V)$, while the components 1 through 3 trace orthogonal degrees of freedom in the extinction curve. In the left panels, the central wavelengths of five previously identified extinction features and one newly identified feature (at 850 nm) are denoted by dashed lines, while the “very broad structure” (VBS) is indicated by a shaded blue region. These four components all modify the strength of the extinction features at 770 and 850 nm, as well as the properties (central wavelength and depth) of the VBS.

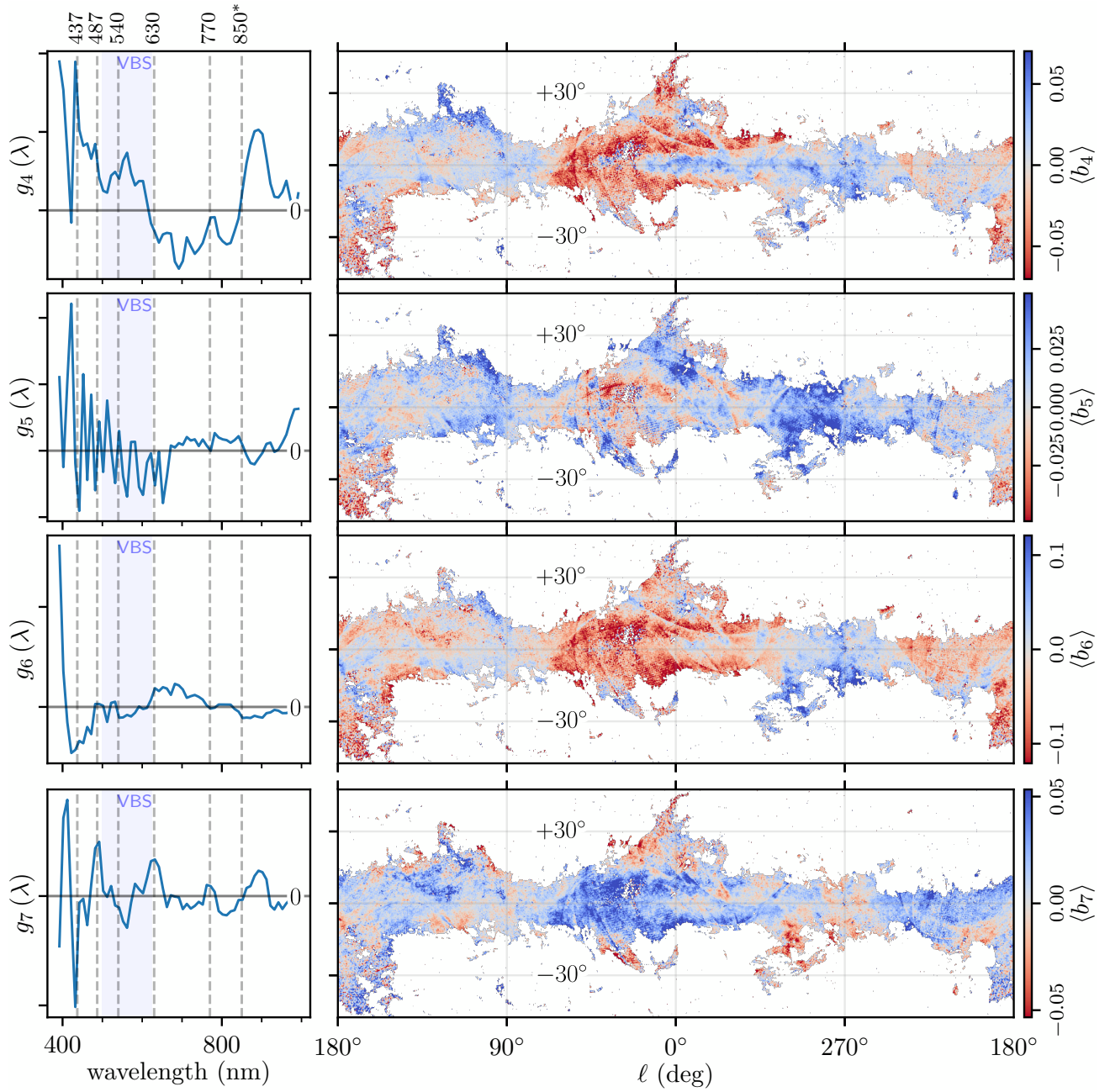


Figure 3. Components 4 through 7 of the extinction curve (left panels), along with sky maps of their mean strengths (right panels). Gaia scanning patterns are visible in these component maps, in the form of long arcs and small checkerboard patterns, though some structures that resemble ISM patterns are still visible.

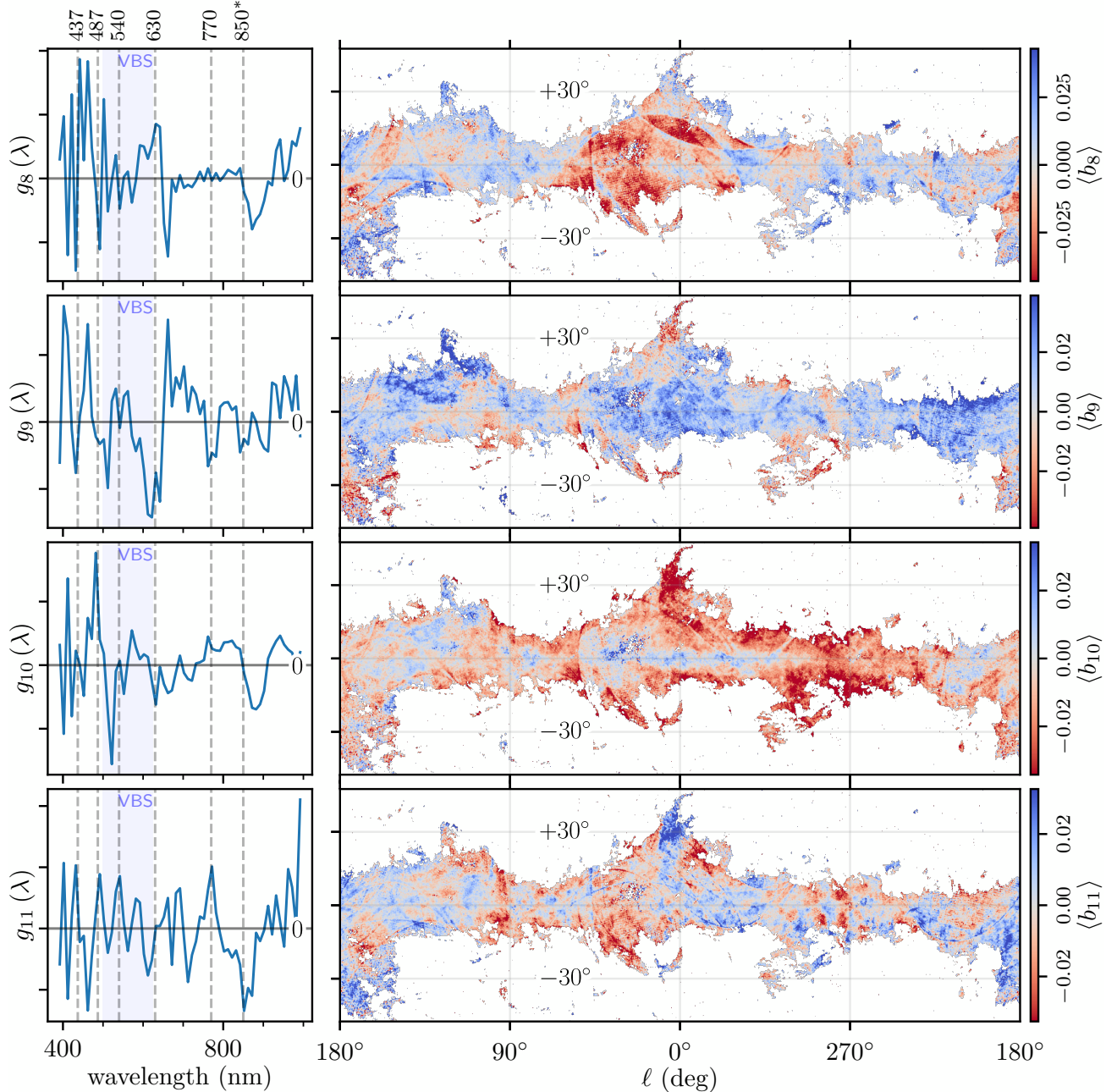


Figure 4. Components 8 through 11 of the extinction curve (left panels), along with sky maps of their mean strengths (right panels). These higher-order components show oscillatory patterns in wavelength that likely capture noise properties of Gaia, and the some of the sky maps show strong Gaia scanning-pattern artifacts. Nevertheless, the sky maps of components 9 and 11 show significant ISM-like structure. Notably, component 11 may contain information about the differential strengths of the 770 and 850 nm extinction features, which are otherwise nearly perfectly correlated.

were \mathbf{C}_i is the covariance matrix of the uncertainties on extinction curve i . We iteratively solve for the basis vectors, \mathbf{G} , and the coefficients, \vec{b}_i . Holding \mathbf{G} constant, there is a linear solution for each \vec{b}_i . Similarly, holding all of the coefficients, \vec{b}_i , constant, there is a linear solution for \mathbf{G} . Before determining the coefficients, \vec{b}_i , we orthogonalize the basis vectors in \mathbf{G} , guaranteeing an orthonormal basis set. χ^2 is quadratic in the

coefficients of both \mathbf{G} and \vec{b}_i , and through repeated iterations, one approaches an optimal solution. We term this process “CovPCA,” and give further details in Appendix B. CovPCA is similar to the approach developed in Tsalmantza & Hogg (2012), with the difference that CovPCA takes into account covariances between measured fluxes at different wavelengths, which is critical for Gaia XP spectra.

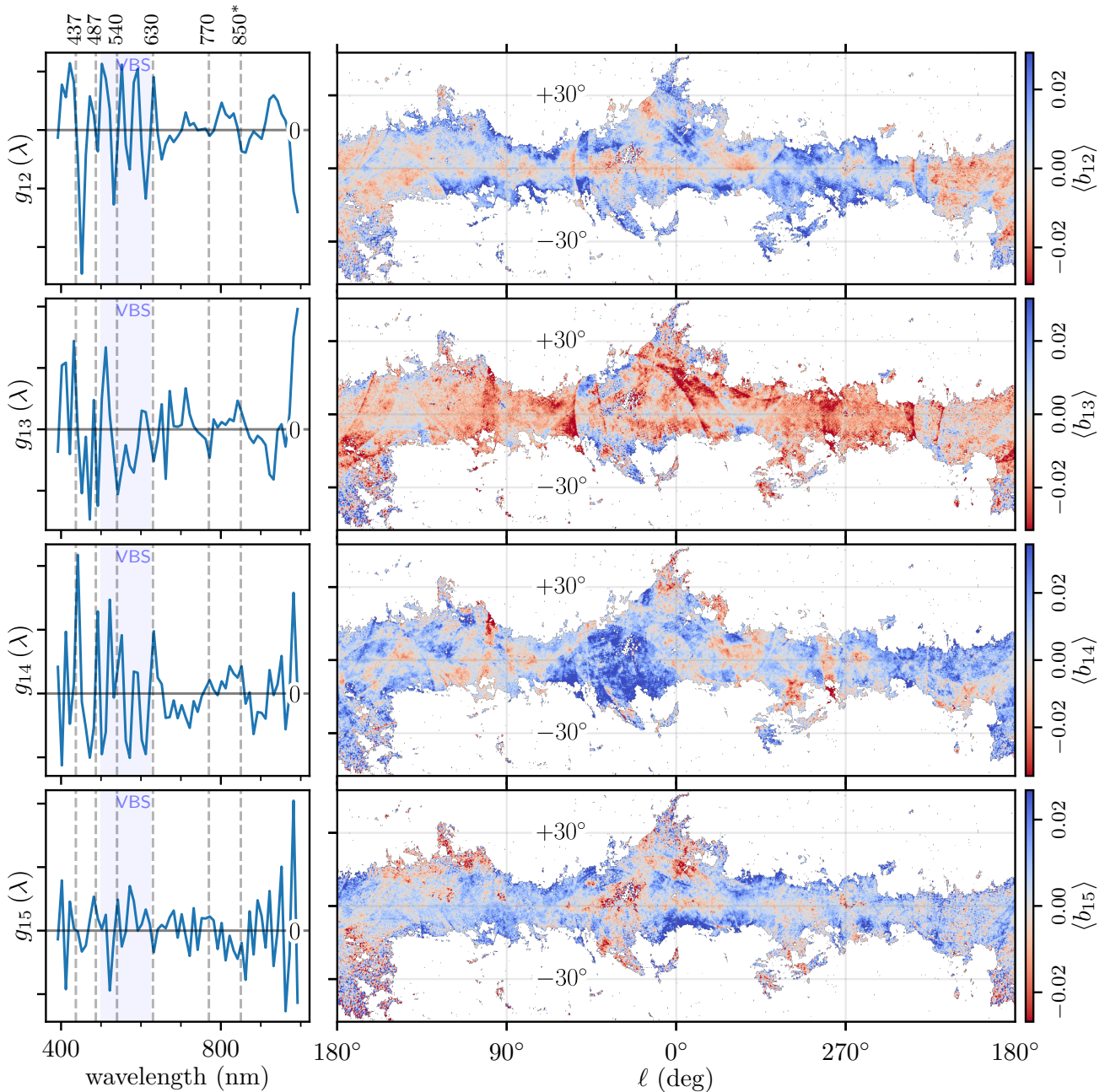


Figure 5. The last four components of the extinction curve (left panels), along with sky maps of their mean strengths (right panels). These components show oscillatory patterns in wavelength, and the sky maps show strong Gaia scanning-pattern artifacts. Some ISM-like structure is still visible in components 12, 14, and 15.

There is an exact $O(n_{\text{dim}})$ degeneracy in the CovPCA solution: any rotation (within the subspace spanned by \mathbf{G}) or reflection of the coefficients \vec{b}_i yields an equivalent solution (under a corresponding transformation of \mathbf{G}). Put more precisely, in Eq. (4), χ^2 only depends on products of the form $\mathbf{G}\vec{b}_i$. If the matrix \mathbf{O} belongs to the orthogonal group $O(n_{\text{dim}})$, then $\mathbf{O}^T = \mathbf{O}^{-1}$, so $\mathbf{G}\mathbf{O}^T\mathbf{O}\vec{b}_i = \mathbf{G}\vec{b}_i$. Transforming $\mathbf{G} \rightarrow \mathbf{G}\mathbf{O}^T$ and every $\vec{b}_i \rightarrow \mathbf{O}\vec{b}_i$ thus leaves χ^2 unchanged. Additionally, unlike

in PCA, the basis vectors in \mathbf{G} are not ordered according to their significance.

In order to obtain a set of basis vectors ordered by significance, we take an iterative approach. We first project all of the extinction curves (and their covariance matrices) down into the 16-dimensional subspace. We then run CovPCA with one dimension to find the basis vector in the subspace that minimizes χ^2 . We term this most significant vector \vec{g}_0 . We then project all of the extinction curves, as well as their covariance matrices,

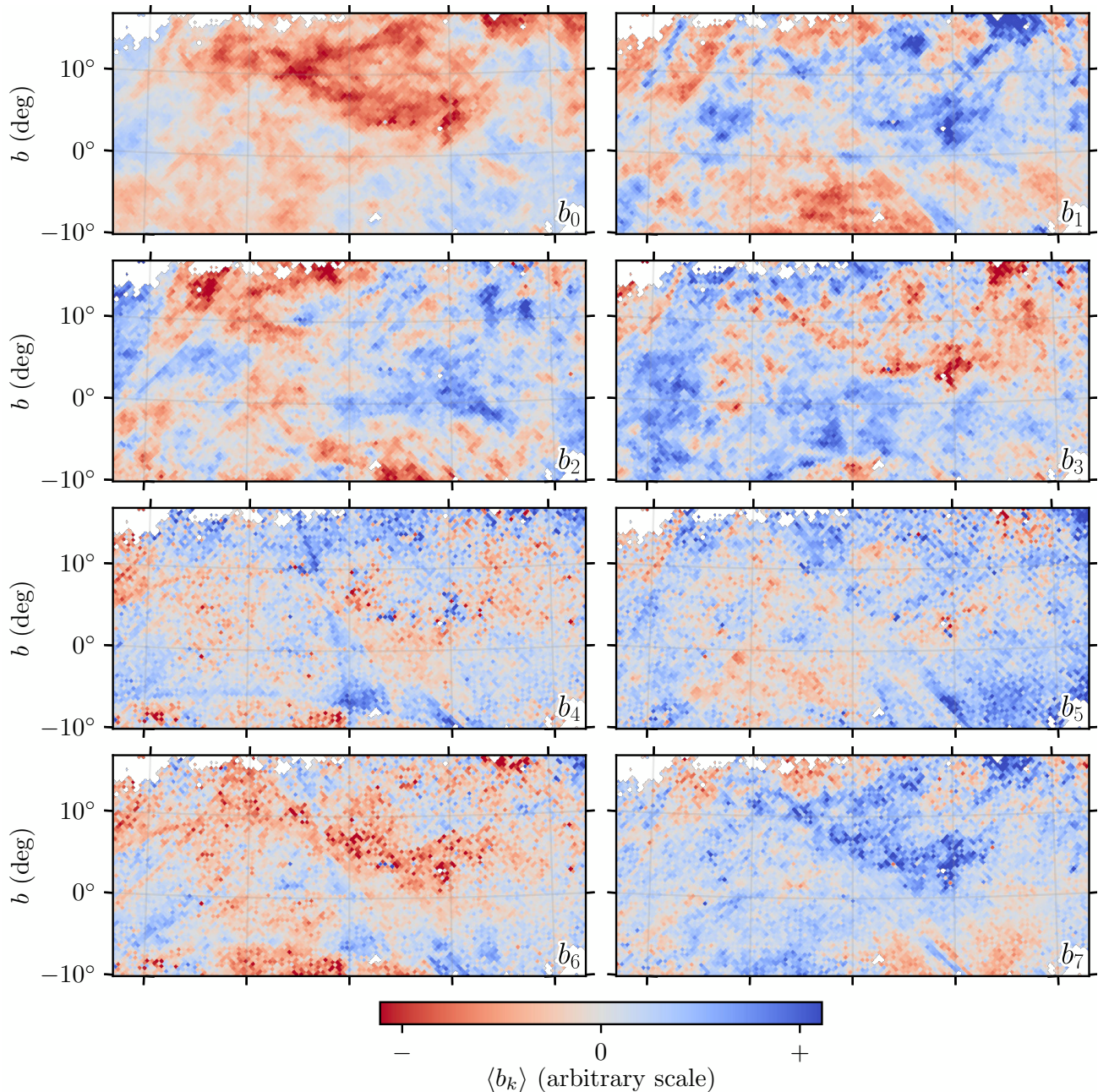


Figure 6. Maps of the mean strength of the first 8 components in the vicinity of Cepheus. The color maps are centered on zero (gray), but the scales are arbitrary, with blue indicating positive values, and red indicating negative values. Components 0-3 show spatial patterns that qualitatively resemble ISM structures, while components 4-7 show strong Gaia scanning-pattern artifacts, in the form of long arcs and checkerboard patterns.

down to a subspace that does not span \vec{g}_0 . We repeat this process, finding the next-most significant basis vector, \vec{g}_1 . We iteratively repeat this procedure until we have n_{dim} basis vectors, which we transform back into the original space and combine into a matrix \mathbf{G} . This iterative process does not fundamentally alter the 16-dimensional subspace originally identified by CovPCA, but simply rotates the basis vectors so that they are ordered by significance. The left panels of Figs. 2–5 shows

the resulting components. We then use \mathbf{G} to solve for the coefficients, \vec{b}_i , that minimize χ^2 . We term this process “iterative CovPCA.”

The left panels of Figs. 2–5 plot our basis vectors, \vec{g}_0 through \vec{g}_{15} , as a function of wavelength. Note that the continuity of our basis vectors in wavelength space comes solely from the data. We do not impose any smoothness regularization on the bases. We discuss the

physical meaning of these basis vectors in the following section.

Having determined a suitable low-dimensional basis that explains most of the variation in HQ extinction curves, we now project a larger set of medium-quality (MQ) extinction curves into this basis. We define MQ in the same way as HQ extinction curves, but with lower thresholds on signal-to-noise ($\text{phot_X_mean_flux}/\text{phot_X_mean_flux_error} > 500$) and extinction ($E > 0.1$). This yields 23.88 million MQ extinction curves. For each MQ extinction curve i , we calculate the coefficients, \vec{b}_i , that minimize χ^2 (Eq. 4), holding the basis, \mathbf{G} , fixed. For each extinction curve, we calculate the resulting χ^2 , as well as a reduced value: $\chi_\nu^2 \equiv \chi^2/(n_{\text{bands}} - n_{\text{dim}})$. This allows us to reject extinction curves that are poorly explained by our subspace.

4. SKY MAPS OF EXTINCTION-CURVE VARIATION

The right panels of Figs. 2–5 show the average strength of each component across the sky. We exclude extinction curves that are poorly represented by our subspace by requiring that $\chi_\nu^2 < 1.5$, and we mask regions of the sky with low average extinction ($E < 0.15$, as determined by ZG24).

Unsurprisingly, component 0 corresponds closely to $R(V)$ as determined by ZG24. However, the subsequent maps show variation in the extinction curve along axes that are orthogonal to $R(V)$ variation. Some of this variation – particularly in higher-order components – is affected by Gaia systematics, as can be seen from sharp arcs and small checkerboard patterns in some of the sky maps. However, the patterns in the four lowest-order component maps (Fig. 2) strongly resemble interstellar medium cloud structure in a qualitative sense, suggesting that these components trace real variation in the extinction curve. Fig. 6 shows zoom-ins of our component maps on the vicinity of Cepheus. We see fine, ISM-like angular structure in the first four components, and strong Gaia scanning-pattern artifacts mixed with some amount of ISM-like structure in the higher-order components.

These component maps demonstrate that there are at least four degrees of freedom that control the shape of the optical extinction curve, and that these degrees of freedom are detectable in Gaia XP spectra.

5. DISTINCT EXTINCTION FEATURES

Three distinct features show up strongly in our extinction curve components 0–3 (see the left panels of Fig. 2): the “very broad structure” (VBS) from roughly 500–625 nm, and two additional extinction features, roughly

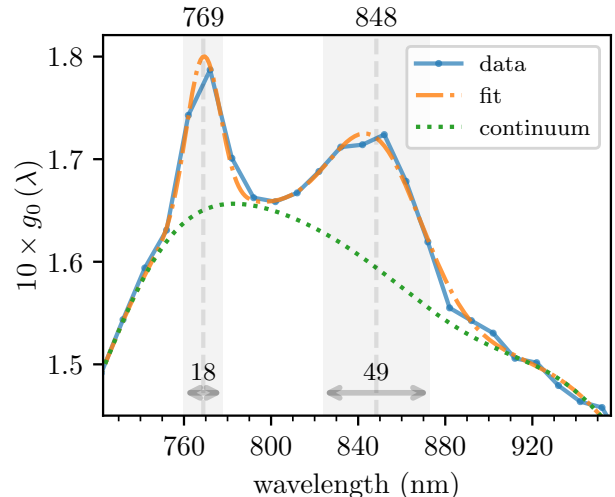


Figure 7. A joint fit of the parameters of the 770 and 850 nm features. As these two features show up prominently in basis vector 0, we model their properties in this basis vector, using the wavelength range 692–982 nm. We treat each feature as a Gaussian profile, and model the continuum as a heavily regularized 11th-order Chebyshev-polynomial expansion. Above, we plot the basis vector \vec{g}_0 (the data) and our fit.

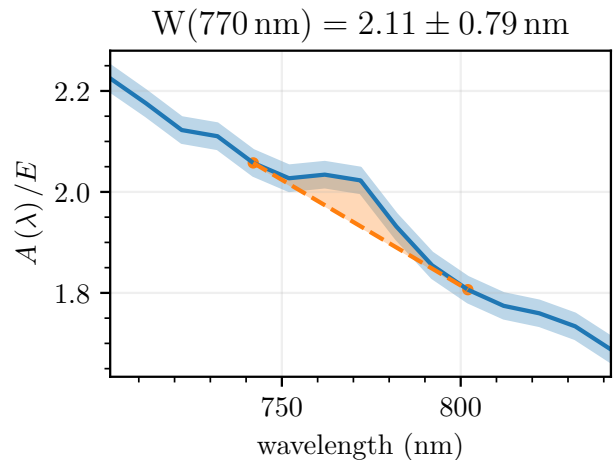


Figure 8. An illustration of the feature-width measurement process for an individual extinction curve. We draw a linear baseline between the edges of the extinction feature in question, as shown by the dotted orange line. The feature width is defined as the integral between the baseline and the normalized extinction curve (represented by the blue curve, with 1σ uncertainties shown in light blue). As the normalized extinction curve is unitless, the resulting integral has units of length. We measure the strength of three features in this manner: the “very broad structure” (VBS), and features at 770 and 850 nm.

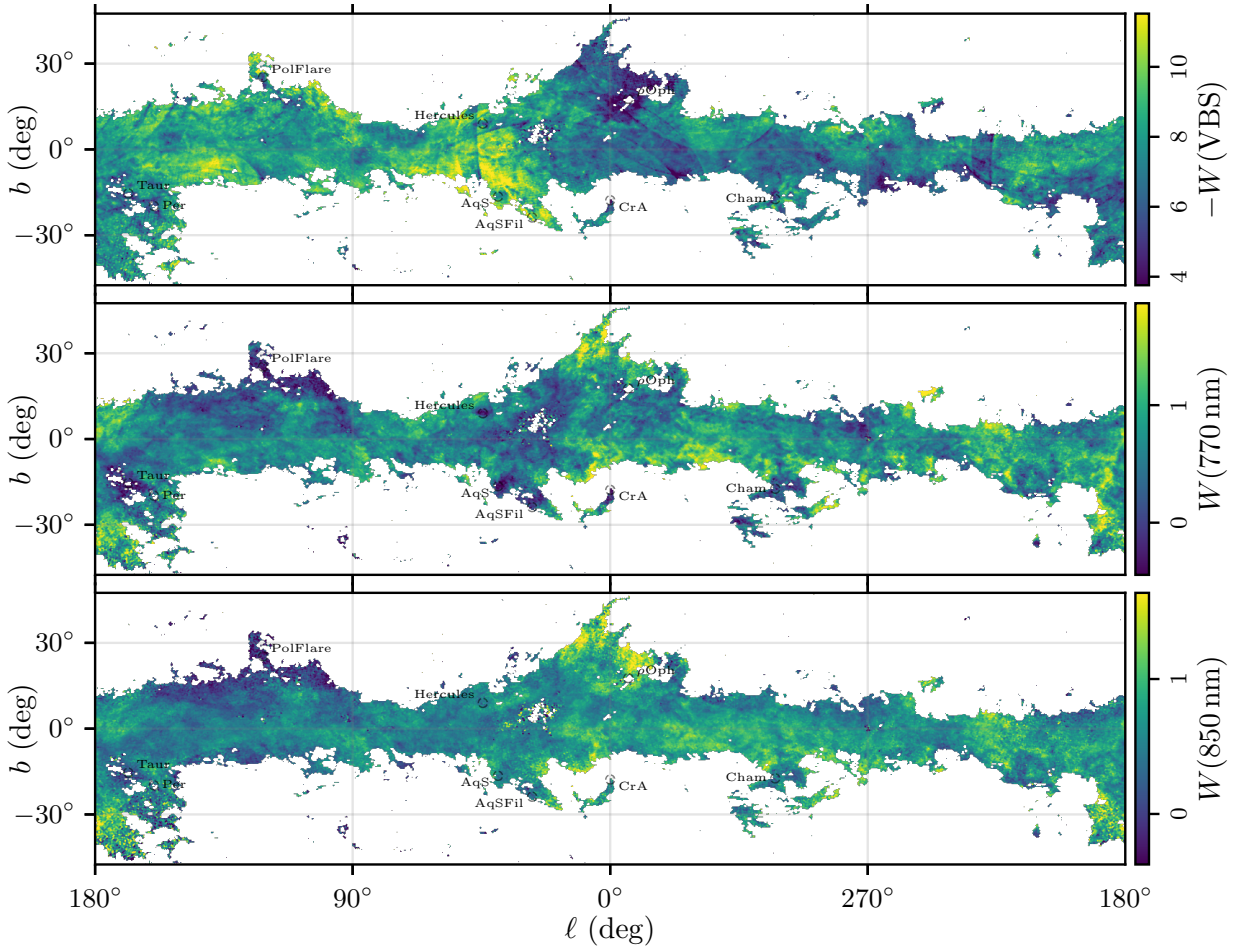


Figure 9. The inverse-variance-weighted mean equivalent width of three prominent features in our extinction curve: the “very broad structure” (VBS), which is a broad depression in extinction, and two bumps in extinction, at 770 and 850 nm. The 770 nm feature was previously identified by Maíz Apellániz et al. (2021) and detected in Gaia XP spectra by Zhang et al. (2024), but the 850 nm feature has not been previously identified. As the VBS is a depression in the extinction curve, we plot its negative equivalent width. All three features show rich structure over the sky. To orient the viewer, we indicate the positions of several dust clouds: Taurus, Perseus, the Polaris Flare, Hercules, Aquila South, filamentary structure near Aquila South, Corona Australis, ρ Ophiuchus, and Chamaeleon. Note that while the maps of $W(770\text{ nm})$ and $W(850\text{ nm})$ are relatively free of Gaia scanning patterns, the map of $-W(\text{VBS})$ is not, possibly due to the greater level of noise in the Gaia XP spectra in the wavelength range of the VBS (see the left panels of Figs. 3–5).

centered on 770 and 850 nm. The 770 nm feature, discovered by Maíz Apellániz et al. (2021) and confirmed by Zhang et al. (2024), shows up in all four of our most significant components, always accompanied by a second feature at 850 nm, which has not been previously identified. As shown in Fig. 7, for the “770 nm” feature, we measure a central wavelength of 769 nm and a full-width at half-maximum (FWHM) of 18 nm, both of which are consistent with the results found by Maíz Apellániz et al. (2021). For the “850 nm” feature, we measure a central wavelength of 848 nm and a FWHM of 49 nm – more than twice as broad as the 770 nm feature, which is itself far broader than any known DIB. For details of this fit, see Appendix D.

We measure the strength of the VBS and the 770 and 850 nm features in each normalized MQ extinction curve. As illustrated in Fig. 8, we define a linear baseline below each feature (anchored at 442 and 802 nm for the 770 nm feature, and at 812 and 892 nm for the 850 nm feature), and then integrate the area between the baseline and the normalized extinction curve. The result has units of length, and is approximately equal to the equivalent width of the feature at an extinction of $E = 1$ (using the ZG24 extinction parameter). As this integral is a linear operation on the extinction curve, the uncertainty on feature width can be easily calculated from the covariance matrix of the extinction curve.

Fig. 9 shows sky maps of the inverse-variance-weighted mean width of each feature on the sky. The correlations

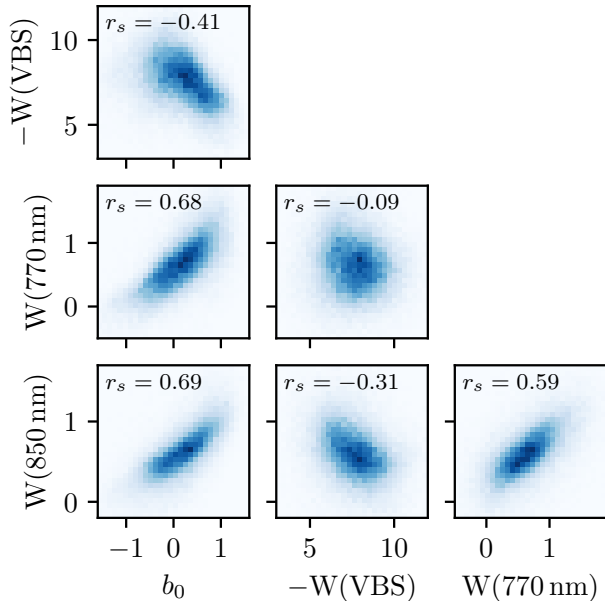


Figure 10. Correlations between the strengths of different features in our sky maps. We compare the amplitude b_0 of basis vector 0 (which represents $R(V)$ variation), and the equivalent widths of the VBS and the 770 and 850 nm features. In each panel, we show the Spearman rank coefficient, r_s , between the two features. A value of +1 indicates perfect correlation, while 0 indicates no correlation and -1 indicates perfect anti-correlation. The 770 and 850 nm features are positively correlated with one another, and both are positively correlated with $R(V)$ (represented above by b_0). The strength of the VBS is anti-correlated with $R(V)$, and is slightly anti-correlated with the 850 nm feature.

between these features are also of great interest, as they might hint that similar chemistry drives the features. Fig. 10 shows the correlations between our sky maps of four features: the amplitude b_0 of basis vector 0 (which represents $R(V)$ variation), and the equivalent widths of the VBS and the 770 and 850 nm features. We see strong positive correlations between $R(V)$ (as measured by b_0) and the strength of the features at 770 and 850 nm, and a strong positive correlation between the strengths of the 770 and 850 nm features. We thus confirm the finding of Massa et al. (2020) that $R(V)$ and the equivalent width of the 770 nm feature are correlated. In our maps, the depth of the VBS is moderately anti-correlated with $R(V)$, slightly anti-correlated with the strength of the 850 nm feature, and has no detectable correlation with the 770 nm feature.

Larger $R(V)$ corresponds to a flatter extinction curve, indicating a larger proportion of large vs. small dust grains. The positive correlation between $R(V)$ and the features at 770 and 850 nm suggests that as small grains become relatively less abundant, the carriers of the 770

and 850 nm features increase in abundance. In order to gain additional insight into the behavior of these features, we calculate the deviation of equivalent width from what one would expect, based on the correlation with $R(V)$. The 16-dimensional subspace representation of the normalized extinction curves is particularly convenient for this purpose. As the equivalent width is a linear transformation of the normalized extinction curve, it can also be expressed as a linear transformation of the coefficients b_i of the basis vectors in our subspace. For example, including the contribution from the mean extinction curve (R_{zp}), we find that the equivalent width of the 770 nm feature is given by $W(770 \text{ nm}) = 0.6342 + 0.3929 b_0 - 3.1316 b_1 + 2.4151 b_2 - 5.7142 b_3$, plus contributions from higher-order components (which we omit here for brevity). As basis vector 0 represents $R(V)$ variation, we can obtain the deviation of equivalent width from the trend with $R(V)$ by only including terms at order b_1 and higher: $\Delta W(770 \text{ nm}) = -3.1316 b_1 + 2.4151 b_2 - 5.7142 b_3 + \dots$.

Fig. 11 plots ΔW for the VBS and 770 and 850 nm features across the sky. The strengths of both the VBS and the 770 nm feature are significantly reduced in the vicinity of ρ Ophiuchus, while the 850 nm features shows no significant reduction in strength in this region. Fig. 12 zooms in on the inner Galaxy, and shows the average extinction curve in two regions near ρ Ophiuchus: one in which the 770 nm feature is suppressed, and another in which the 850 nm feature is stronger than other sightlines with comparable $R(V)$. One possible explanation for this behavior would be if the carrier of the 770 nm feature undergoes photodissociation from the intense UV radiation environment in the ρ Ophiuchus region. This finding is in line with Maíz Apellániz et al. (2021), which found that the equivalent width of the 770 nm feature is suppressed in star-forming regions with O/B associations. Massa et al. (2020) argue that the VBS is the result of the extinction peaks at 487 and 630 nm, representing a minimum between these two features. If this is true, a reduction in the depth of the VBS corresponds to a reduction in the strength of the 487 and 630 nm features, and the carriers of these features may also be destroyed in regions with strong UV radiation.

We now pose the question of the reality of the 850 nm feature. The 850 nm feature shows up not only in Gaia XP extinction curves – it can be seen (as can the 770 nm feature) in Fig. 5 of Gordon et al. (2023, “G23”), which plots the residuals between the measured and modeled mean extinction curve (which they label “ $a - \text{fit}$ ”). G23 notes, however, that this region of the spectrum could be affected by the Paschen jump, which occurs at 820.4 nm. There are three reasons why we do not be-

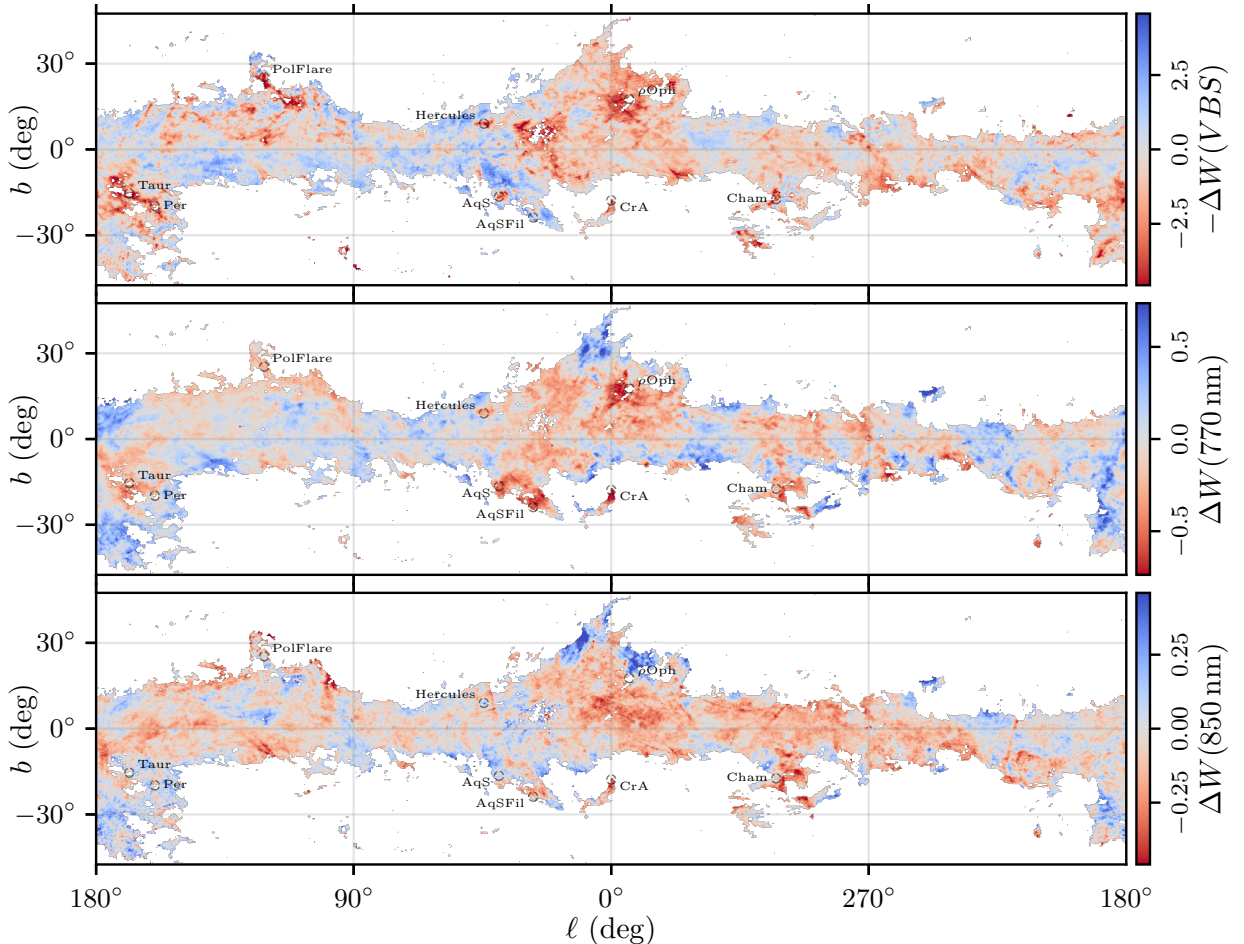


Figure 11. Sky maps of the mean difference in equivalent width of the VBS, 770 nm and 850 nm features from what one would expect, based on their correlation with $R(V)$. The strengths of these three features are not perfectly correlated with $R(V)$, and indeed we see spatial patterns in the residuals that have ISM-like structure. Notably, we see strong reductions in the equivalent widths of the VBS and 770 nm features (but not of the 850 nm feature) in the vicinity of ρ Ophiuchus, a star-forming region with several O/B-star associations and a strong UV radiation field. This may hint at photodissociation of the carriers of these features.

lieve the Paschen series to be responsible for the 850 nm feature. The first reason is that the sky map of this feature show ISM-like spatial patterns, and is indeed highly correlated with the sky map of the 770 nm feature, which cannot be affected by the Paschen series, as well as the sky map of b_0 , which traces $R(V)$ and should be fairly insensitive to the Paschen lines. The top panels of Fig. 12 zoom in on these three features (and the VBS) near the Galactic Center, showing that they trace similar (but not identical) ISM-like structure. The second reason is that restricting our stellar sample to low-temperature stars ($T_{\text{eff}} < 6000$ K), for which the Paschen lines should be very weak, leaves the sky map of W (850 nm) nearly unchanged. A third, related reason is that on a star-by-star basis, W (850 nm) is uncorrelated with T_{eff} . Using MQ extinction curves with uncertainty of less than 0.75 nm in effective width, we measure a

Pearson rank correlation coefficient of -0.129 with T_{eff} , as compared to much stronger correlation coefficients of 0.592 with $R(V)$ and 0.342 with W (770 nm) (note that this star-by-star comparison is noisier than the comparison shown in Fig. 10, which are based on sky maps of average feature strengths). Finally, we note that the 850 nm feature can also be seen in Fig. 5 of Zhang et al. (2024, “Zh24”), and is particularly clear in the residuals between their model and that of G23. While the Zh24 extinction curves are also measured using XP, and therefore share the same Gaia systematics as our extinction curves, their method of determining the intrinsic stellar spectrum (*i.e.*, pairing with unreddened analogs using LAMOST spectra) is completely different.

6. DISCUSSION OF THE ORIGINS OF THE 770 AND 850 NM FEATURES

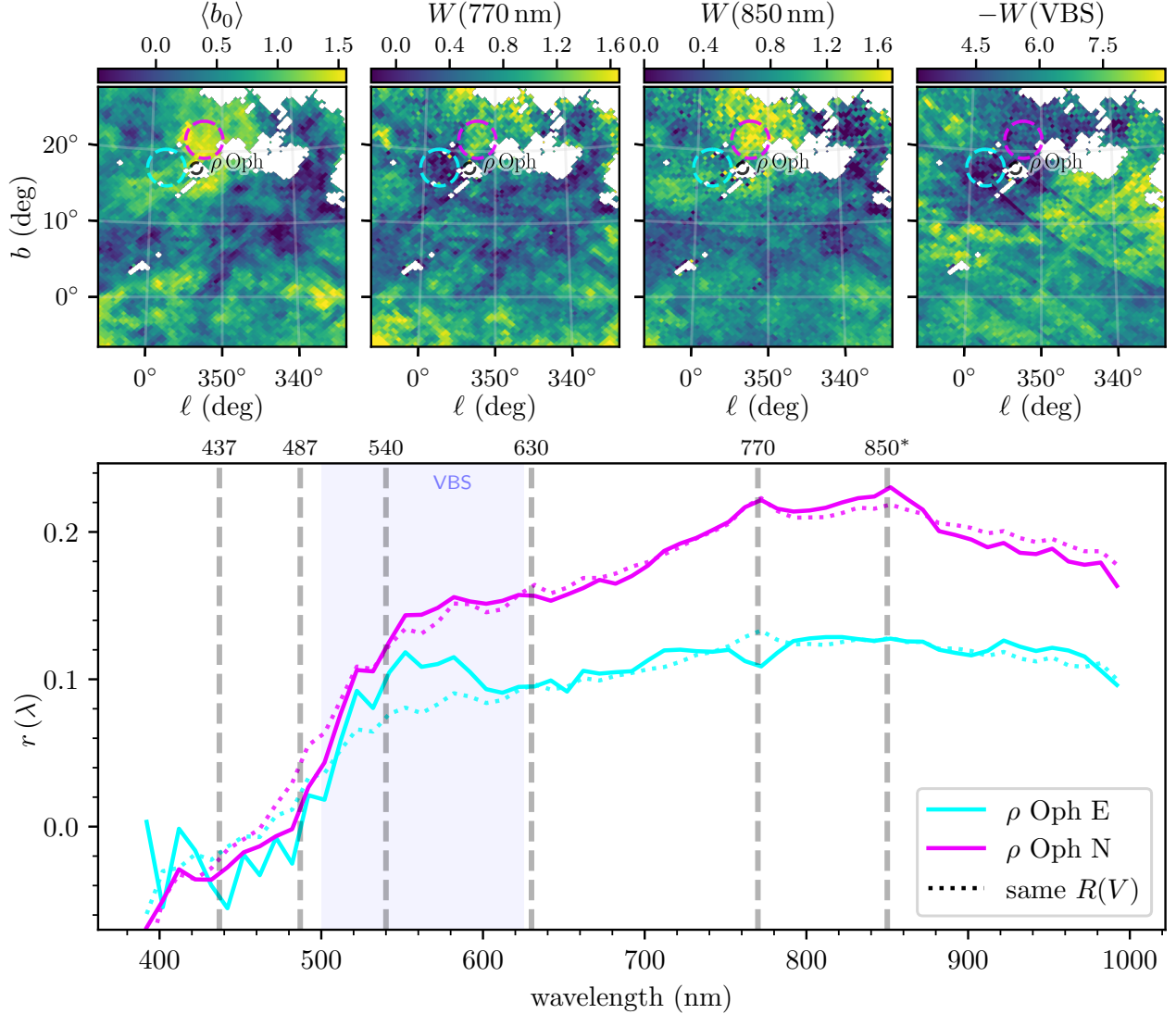


Figure 12. Top panels: Sky maps of $\langle b_0 \rangle$ (which traces $R(V)$), the 770 and 850 nm features and the VBS in the direction of the inner Galaxy. The first three features trace similar – but not identical – structure, which has typical ISM-like filaments and cloud structures. The depth of the VBS is anti-correlated with the first three features. The largest differences between the maps are in the vicinity of ρ Ophiuchus, where intense UV radiation from nearby O/B associations should strongly affect the dust chemistry. Bottom panel: The mean extinction curve (centered by subtracting the mean of the extinction curve across the entire sky) in two circled regions, North and East of ρ Ophiuchus. The extinction curve in the region North of ρ Ophiuchus shows a stronger 850 nm feature than other areas of the sky with an equivalent $R(V)$ (shown by the dotted line of the same color). The region East of ρ Ophiuchus shows a much reduced 750 nm feature compared to other regions of the sky with the same $R(V)$, as well as a shallower VBS (as can be seen from the difference between the solid and dotted cyan lines in the wavelength range of the VBS). The particular behavior in both of these regions illustrates that $R(V)$ is insufficient to fully describe the extinction curve, and that the dust in different regions with the same $R(V)$ can have different chemical composition.

Zhang *et al.* (2024; “ZHG24”; *in preparation*) argues that much of the $R(V)$ variation in the translucent ISM of the Milky Way and LMC is driven by variations in PAH abundance. PAHs are thought to be abundant in the ISM (*e.g.*, Wenzel *et al.* 2024a,b), and generically contain an electronic $\pi \leftrightarrow \pi^*$ transition in the UV that may be the origin of the 2175 Å feature (Draine 2003). Though the center of this feature is in the UV,

its long-wavelength wing extends into the optical, where it steepens the extinction curve. An increase in PAH mass fraction (compared to the total dust mass) from 4% to 8%, which is allowed by the carbon budget in the gas phase of the diffuse ISM, is sufficient to reduce $R(V)$ from 3.4 to 2.9 (Zhang *et al.* 2024; *in preparation*), and indeed just such a trend is seen in several clouds studied by ZHG24.

In this picture, destruction of PAHs (for example, by UV radiation) increases $R(V)$, while growth of PAHs through accretion of carbon from the gas phase causes $R(V)$ to decrease (Zhang *et al.* 2024; *in preparation*). In this work, we see an increase in the strength of the 770 and 850 nm features as $R(V)$ increases (see Fig. 10). This lends itself to the conjecture that the carriers of the 770 and 850 nm features are small carbon-bearing molecules that become more abundant in environments where PAHs are destroyed. As seen in Figs. 11 and 12, the 770 nm feature is suppressed in the vicinity of ρ Ophiuchus, which is a region with several O/B associations and thus, a particularly strong UV radiation field. In this environment, the carrier (or carriers) of the 770 nm feature may also undergo photodissociation. The 850 nm feature shows no such suppression near ρ Ophiuchus, possibly indicating that its carrier (or class of carriers) is more stable.

Maíz Apellániz *et al.* (2021) found that the 770 nm feature is weaker along sightlines that are rich in diatomic carbon, C_2 , indicating some connection to carbon chemistry. However, absent specifically identified carriers with transitions at the correct energies, and absent identification of additional transitions belonging to these carriers (e.g., rotational transitions in the radio spectrum), this conjecture is highly tentative.

7. CONCLUSIONS

Though the optical extinction curve has commonly been assumed to be described by a single parameter, $R(V)$, the availability of large numbers measured extinction curves – determined using low-resolution Gaia

XP spectra – reveals additional physical degrees of freedom that are richly structured on the sky.

In this paper, we identify a new, broad optical extinction feature centered on $\lambda \approx 848$ nm (the “850 nm” feature), with a FWHM of 49 nm (several times the width of the broadest known DIB). We measure the equivalent widths of the VBS and the 770 and 850 nm features in 24 million extinction curves, allowing us to map the strength of each feature across the sky. These features show strong correlations with one another and with $R(V)$. However, $R(V)$ is insufficient to predict the strength of these features in every environment. For example, in the vicinity of ρ Ophiuchus, where there are a number of O/B associations and a history of recent (~ 20 Myr) star formation (Ratzenböck *et al.* 2023), the 770 nm feature is significantly weaker than one would expect, based on its overall correlation with $R(V)$, indicating possible photodissociation of its carrier by intense UV radiation. By contrast, the 850 nm feature does not show a deficit in this same region.

Our extinction curve decompositions and equivalent-width measurements for the VBS and 770 and 850 nm features are available at DOI:10.5281/zenodo.14005028. The large catalog, densely covering the entire Galactic plane, will allow more detailed investigation of connections between optical extinction features and ISM conditions and chemistry.

ACKNOWLEDGMENTS

GG and XZ are supported by a Sofja Kovalevskaja Award to GG from the Humboldt Foundation. We have had useful conversations about some of the results in this paper with Brandon Hensley, Christiaan Boersma, Vincent Esposito and Alexandros Maragkoudakis.

REFERENCES

- Cardelli, J. A., Clayton, G. C., & Mathis, J. S. 1989, *ApJ*, 345, 245, doi: [10.1086/167900](https://doi.org/10.1086/167900)
- De Angeli, F., Weiler, M., Montegriffo, P., *et al.* 2023, *A&A*, 674, A2, doi: [10.1051/0004-6361/202243680](https://doi.org/10.1051/0004-6361/202243680)
- Draine, B. T. 2003, *ARA&A*, 41, 241, doi: [10.1146/annurev.astro.41.011802.094840](https://doi.org/10.1146/annurev.astro.41.011802.094840)
- Fitzpatrick, E. L. 1999, *PASP*, 111, 63, doi: [10.1086/316293](https://doi.org/10.1086/316293)
- Gaia Collaboration, Prusti, T., de Bruijne, J. H. J., *et al.* 2016, *A&A*, 595, A1, doi: [10.1051/0004-6361/201629272](https://doi.org/10.1051/0004-6361/201629272)
- Gaia Collaboration, Vallenari, A., Brown, A. G. A., *et al.* 2023, *A&A*, 674, A1, doi: [10.1051/0004-6361/202243940](https://doi.org/10.1051/0004-6361/202243940)
- Gordon, K. D., Clayton, G. C., Declair, M., *et al.* 2023, *ApJ*, 950, 86, doi: [10.3847/1538-4357/acb59](https://doi.org/10.3847/1538-4357/acb59)
- Maíz Apellániz, J., Barbá, R. H., Caballero, J. A., Bohlin, R. C., & Fariña, C. 2021, *MNRAS*, 501, 2487, doi: [10.1093/mnras/staa2371](https://doi.org/10.1093/mnras/staa2371)
- Massa, D. 1980, *AJ*, 85, 1651, doi: [10.1086/112844](https://doi.org/10.1086/112844)
- Massa, D., Fitzpatrick, E. L., & Gordon, K. D. 2020, *ApJ*, 891, 67, doi: [10.3847/1538-4357/ab6f01](https://doi.org/10.3847/1538-4357/ab6f01)
- Montegriffo, P., De Angeli, F., Andrae, R., *et al.* 2023, *A&A*, 674, A3, doi: [10.1051/0004-6361/202243880](https://doi.org/10.1051/0004-6361/202243880)
- Peek, J. E. G., & Schiminovich, D. 2013, *ApJ*, 771, 68, doi: [10.1088/0004-637X/771/1/68](https://doi.org/10.1088/0004-637X/771/1/68)
- Ratzenböck, S., Großschedl, J. E., Alves, J., *et al.* 2023, *A&A*, 678, A71, doi: [10.1051/0004-6361/202346901](https://doi.org/10.1051/0004-6361/202346901)
- Schlafly, E. F., Peek, J. E. G., Finkbeiner, D. P., & Green, G. M. 2017, *ApJ*, 838, 36, doi: [10.3847/1538-4357/aa619d](https://doi.org/10.3847/1538-4357/aa619d)

Schlafly, E. F., Meisner, A. M., Stutz, A. M., et al. 2016, ApJ, 821, 78, doi: [10.3847/0004-637X/821/2/78](https://doi.org/10.3847/0004-637X/821/2/78)

Tsalmantza, P., & Hogg, D. W. 2012, ApJ, 753, 122, doi: [10.1088/0004-637X/753/2/122](https://doi.org/10.1088/0004-637X/753/2/122)

Wenzel, G., Cooke, I. R., Changala, P. B., et al. 2024a, arXiv e-prints, arXiv:2410.00657, doi: [10.48550/arXiv.2410.00657](https://doi.org/10.48550/arXiv.2410.00657)

Wenzel, G., Speak, T. H., Changala, P. B., et al. 2024b, arXiv e-prints, arXiv:2410.00670, doi: [10.48550/arXiv.2410.00670](https://doi.org/10.48550/arXiv.2410.00670)

Zhang, R., Yuan, H., Huang, B., et al. 2024, ApJ, 971, 127, doi: [10.3847/1538-4357/ad613e](https://doi.org/10.3847/1538-4357/ad613e)

Zhang, X., & Green, G. 2024, arXiv e-prints, arXiv:2407.14594, doi: [10.48550/arXiv.2407.14594](https://doi.org/10.48550/arXiv.2407.14594)

APPENDIX

A. EFFECT OF OBSERVATIONAL UNCERTAINTIES ON ESTIMATED EXTINCTION

When both the intrinsic and observed (f_{obs}) flux are known exactly, extinction is simply given by

$$A = -2.5 \log_{10} \left(\frac{f_{\text{obs}}}{f_{\text{int}}} \right). \quad (\text{A1})$$

However, when f_{obs} contains observational uncertainties, there are corrections to the above formula. When the observational uncertainties are Gaussian, these corrections take the form of a power series in the inverse of the signal-to-noise ratio, σ_f/μ_f . To see why this is, consider the expected value of $y = \ln(x)$, where x is a Gaussian random variable with mean μ and standard deviation σ . Defining $z \equiv (x - \mu)/\sigma$,

$$\langle y \rangle = \langle \ln(x) \rangle = \langle \ln(\mu + \sigma z) \rangle = \ln \mu + \langle \ln \left(1 + \frac{\sigma}{\mu} z \right) \rangle. \quad (\text{A2})$$

Expanding the natural logarithm as a Taylor series,

$$\langle y \rangle = \ln \mu + \sum_{k=1}^{\infty} \frac{(-1)^k}{k} \left(\frac{\sigma}{\mu} \right)^k \langle z^k \rangle. \quad (\text{A3})$$

As z is a unit Gaussian random variable, its odd moments are zero, and its even moments are given by $(k-1)!!$. Thus,

$$\langle y \rangle = \ln \mu + \sum_{k=2,4,6,\dots} \frac{(-1)^k}{k} \left(\frac{\sigma}{\mu} \right)^k (k-1)!! \quad (\text{A4})$$

$$= \ln \mu + \sum_{n=1}^{\infty} \frac{(2n-1)!!}{2n} \left(\frac{\sigma}{\mu} \right)^{2n}. \quad (\text{A5})$$

Applying this formula to the definition of extinction and Keeping only the lowest-order term in the series expansion yields Eq. 1. The series in Eq. A5 is asymptotic, and diverges as $n \rightarrow \infty$. However, for reasonably small σ/μ , it becomes more accurate as one adds in low-order terms.

A similar approach can be used to obtain the covariance $\text{cov}(y_1, y_2)$, where $y_i = \ln(x_i)$, and x_1 and x_2 are correlated Gaussian random variables:

$$\text{cov}(y_1, y_2) \simeq \left(\frac{\sigma_{1,2}^2}{\mu_1 \mu_2} - \frac{1}{4} \frac{\sigma_1^2 \sigma_2^2}{\mu_1^2 \mu_2^2} \right), \quad (\text{A6})$$

where $\sigma_{1,2}^2$ is the covariance between x_1 and x_2 .

B. COVPCA ALGORITHM

We have observations of extinction curves, \vec{A}_i (i is the index of stars), each with its own covariance matrix, \mathbf{C}_i . We want to find a set of ndim basis vectors, represented by the basis matrix G_{jk} , that minimizes χ^2 :

$$\chi^2 = \sum_{i,j,k,l,m} (G_{jk} B_{i,k} - A_{i,j}) (C_i^{-1})_{jl} (G_{lm} B_{i,m} - A_{i,l}), \quad (\text{B7})$$

where \vec{B}_i is the coefficient representation of extinction curves in the space spanned by $\mathbf{G}_{\text{nbands} \times \text{ndim}}$. However, it is difficult to simultaneously determine $\mathbf{G}_{\text{nbands} \times \text{ndim}}$ and $\mathbf{B}_{\text{ndim} \times \text{nstar}}$. We alternatively adopt an iterative method.

B.1. *B-step: Assume matrix G is known.*

To minimize χ^2 w.r.t. the coefficients, \mathbf{B} , holding the basis vectors fixed, we require

$$\frac{\partial \chi^2}{\partial B_{i,p}} = 0. \quad (\text{B8})$$

$$\implies 0 = \sum_{j,k,l,m} [G_{jp}(C_i^{-1})_{jl}(G_{lm}B_{i,m} - A_{i,l}) + (G_{jk}B_{i,k} - A_{i,j})(C_i^{-1})_{jl}G_{lp}]. \quad (\text{B9})$$

If we re-label the dummy indices of the second term: ($j \rightarrow l$, $l \rightarrow j$, $k \rightarrow m$), we find it is identical with the first term:

$$0 = \sum_{j,k,l,m} [G_{jp}(C_i^{-1})_{jl}(G_{lm}B_{i,m} - A_{i,l}) + (G_{lm}B_{i,m} - A_{i,l})(C_i^{-1})_{jl}G_{jp}], \quad (\text{B10})$$

$$\sum_{j,k,l,m} G_{jp}(C_i^{-1})_{jl}(G_{lm}B_{i,m} - A_{i,l}) = 0. \quad (\text{B11})$$

In matrix notation, this is:

$$\mathbf{G}^T \mathbf{C}_i^{-1} \mathbf{G} \vec{B}_i = \mathbf{G}^T \mathbf{C}_i^{-1} \vec{A}_i \quad (\text{B12})$$

Note that $\mathbf{G}^T \mathbf{C}_i^{-1} \mathbf{G}$ is always invertible. Thus, the optimal coefficients are given by

$$\vec{B}_i = (\mathbf{G}^T \mathbf{C}_i^{-1} \mathbf{G})^{-1} \mathbf{G}^T \mathbf{C}_i^{-1} \vec{A}_i. \quad (\text{B13})$$

B.2. *G-step: Assume matrix B is known.*

Similarly, in order to minimize χ^2 w.r.t. the basis vectors, holding the coefficients constant, we require,

$$\frac{\partial \chi^2}{\partial G_{pq}} = 0. \quad (\text{B14})$$

$$\implies 0 = \sum_{i,j,k,l,m} [B_{i,q}(C_i^{-1})_{pl}(G_{lm}B_{i,m} - A_{i,l}) + (G_{jk}B_{i,k} - A_{i,j})(C_i^{-1})_{jp}B_{i,q}]. \quad (\text{B15})$$

The second term is also the same as the first term if we re-label the dummy indices ($j \rightarrow l$, $k \rightarrow m$). Thus,

$$0 = \sum_{i,l,m} B_{i,q}(C_i^{-1})_{pl}(G_{lm}B_{i,m} - A_{i,l}). \quad (\text{B16})$$

This gives us $\mathbf{nbands} \times \mathbf{ndim}$ equations.

We flatten the G matrix into a vector: $\mathbf{G}'_{\mathbf{a}}$

$$G'_a = G_{lm}, \quad (\text{B17})$$

where $m = \text{floor}(a/\mathbf{nbands})$, $l = a \bmod \mathbf{nbands}$.

We can also flatten other matrices by $q = \text{floor}(b/\mathbf{nband})$, $p = b \bmod \mathbf{nbands}$:

$$A'_{ba} G'_a = R'_b, \quad (\text{B18})$$

$$A'_{ba} = \sum_i B_{i,q}(C_i^{-1})_{pl} B_{im}, \quad (\text{B19})$$

$$R'_b = \sum_{i,l} B_{i,q}(C_i^{-1})_{pl} A_{il}. \quad (\text{B20})$$

Therefore, we can calculate G' by

$$G' = (A')^{-1} R'. \quad (\text{B21})$$

Reshaping G' yields the basis matrix, \mathbf{G} .

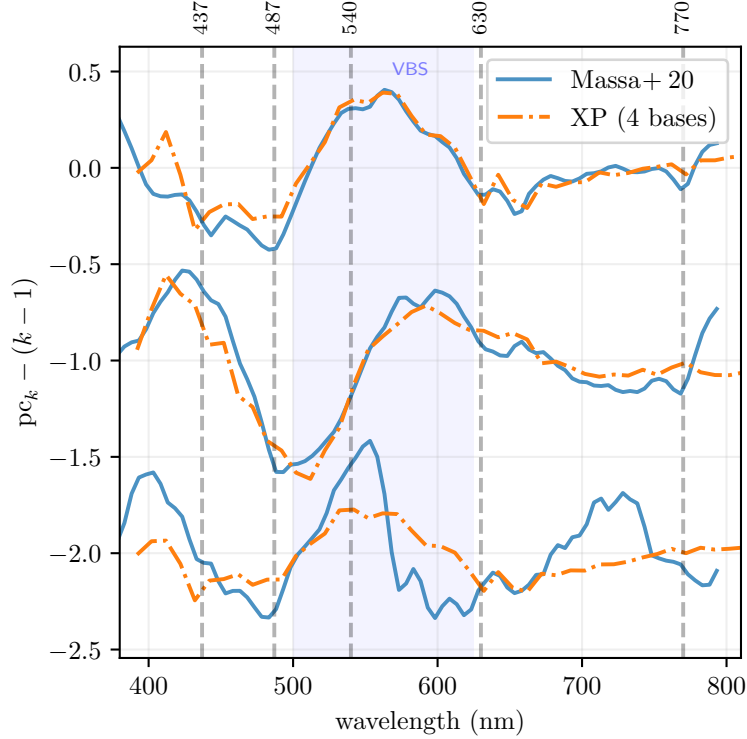


Figure 13. Comparison of the extinction curve principal components found by Massa et al. (2020, “MFG20”) (in order of most to least significance from top to bottom) with our lowest-order basis vectors. For each MFG20 principal component, we overplot the best-matching linear combination of our four most significant basis vectors (labeled “XP”). Our four most significant basis vectors capture the variation encoded by MFG20’s pc_1 and pc_2 , but not the variation encoded by pc_3 . This latter variation is distributed over our higher-order basis vectors. Note that the wavelength range of our basis vectors and that of MFG20’s principal components are not identical – we plot the overlap region.

B.3. Covariance matrix of basis vectors

We can calculate the covariance matrix of each basis vector, \vec{B} , using the fact that it is a linear transformation of the corresponding vector \vec{A} :

$$\vec{B} = \underbrace{(\underbrace{\mathbf{G}^T \mathbf{C}^{-1} \mathbf{G}}_{\equiv \mathbf{J}})^{-1} \mathbf{G}^T \mathbf{C}^{-1}}_{\equiv \mathbf{K}} \vec{A} = \mathbf{K} \vec{A}. \quad (\text{B22})$$

Note that $\mathbf{J} = \mathbf{J}^T$. The covariance matrix of \vec{B} is then given by

$$C_B = \mathbf{K} \mathbf{C} \mathbf{K}^T = \mathbf{J}^{-1} \mathbf{G}^T \underbrace{\mathbf{C}^{-1} \mathbf{C}}_{=1} (\mathbf{J}^{-1} \mathbf{G}^T \mathbf{C}^{-1})^T = \mathbf{J}^{-1} \underbrace{\mathbf{G}^T \mathbf{C}^{-1} \mathbf{G}}_{=1} \mathbf{J}^{-1} = \mathbf{J}^{-1} \quad (\text{B23})$$

$$= (\mathbf{G}^T \mathbf{C}^{-1} \mathbf{G})^{-1}. \quad (\text{B24})$$

C. COMPARISON WITH MASSA *ET AL.* (2020)

Massa et al. (2020, “MFG20”) applied principal component analysis to extinction curves calculated from observed Hubble/STIS optical spectra, obtaining three statistically significant components. We compare these principal components to our basis vectors, which are obtained by applying CovPCA to the Gaia XP extinction curves.

Because the principal components of MFG20 could be a linear combination of our basis vectors, we find the combination of our basis vectors that minimizes the mean square difference with each MFG20 principal component, pc_k , $k = 1, 2, 3$. As our space of basis vectors is very large (16 dimensions) compared to the three principal components of MFG20, we only use our four most significant basis vectors in this comparison. This essentially tests whether the

same extinction-curve variations seen by MFG20 are captured by our lowest-order basis vectors. We find the following transformations:

$$pc_1 \simeq +0.0900 \vec{g}_0 + 0.3448 \vec{g}_1 - 0.2283 \vec{g}_2 - 0.2400 \vec{g}_3, \quad (C25)$$

$$pc_2 \simeq -0.1514 \vec{g}_0 + 0.4230 \vec{g}_1 + 0.4646 \vec{g}_2 - 0.0828 \vec{g}_3, \quad (C26)$$

$$pc_3 \simeq -0.0152 \vec{g}_0 + 0.1550 \vec{g}_1 - 0.1868 \vec{g}_2 - 0.2090 \vec{g}_3. \quad (C27)$$

$$(C28)$$

Fig. 13 plots our transformed basis vectors on top of the MFG20 principal components. We recover the first two principal components of MFG20 fairly closely, but the third principal component of MFG20 evidently contains extinction-curve variation that cannot be captured by our lowest-order principal components. Interestingly, the 770 nm feature is visible in the first two MFG20 principal components, although it was only identified later, by Maíz Apellániz et al. (2021).

D. DETAILS OF JOINT 770 AND 850 NM FEATURE FIT

As illustrated in Fig. 7, we perform a joint fit of the properties of the 770 and 850 nm features in our basis vector 0 (which represents $R(V)$ variation). This requires us to also model the continuum of basis vector 0. We model each feature as a Gaussian profile (with amplitude a , central wavelength $\bar{\lambda}$, and width $\Delta\lambda$), and the continuum as an 11th-order Chebyshev-polynomial expansion:

$$r_{\text{pred}}(\lambda) \simeq \sum_{i=1}^2 a_i \exp \left[-\frac{(\lambda - \bar{\lambda}_i)^2}{2(\Delta\lambda_i)^2} \right] + \sum_{i=0}^{11} c_i T_i \left(\frac{\lambda - 837 \text{ nm}}{145 \text{ nm}} \right), \quad (D29)$$

where T_i is the i^{th} -order Chebyshev polynomial, c_i is the corresponding fitting coefficient, and we model the range 792–982 nm. We first obtain a rough fit by minimizing $\langle [r_{\text{pred}}(\lambda) - g_0(\lambda)]^2 \rangle$, holding c_6 through c_{11} fixed at zero. This leads to a fit with a root-mean-square error of $\sigma_{\text{rms}} = 5.56 \times 10^{-4}$.

Visual inspection shows that the resulting continuum fit contains moderately strong undulations that appear unphysical. We then re-run the fit, using the rough fit as a starting point, but allowing the higher-order Chebyshev polynomial coefficients to vary, and heavily regularizing all terms above order c_2 . We minimize the objective function

$$\mathcal{L} = \frac{1}{2\sigma_{\text{rms}}^2} \sum_{i=1}^{n_\lambda} [r_{\text{pred}}(\lambda_i) - g_0(\lambda_i)]^2 + 10^6 \sum_{i=3}^{11} c_i^2, \quad (D30)$$

where $n_\lambda = 30$ is the number of modeled wavelengths, and $\lambda_i = 692 \text{ nm}, 702 \text{ nm}, \dots, 982 \text{ nm}$. We obtain the fit shown in Fig. 7.

The central wavelengths and FWHM of the 770 and 850 nm features are largely insensitive to the details of the continuum fit, and change by less than 1 nm from our rough fit to our final fit. However, the amplitudes of the features are affected by the details of the continuum fit.